Bull Volcanol (2006) 68: 240–254
DOI 10.1007/s00445-005-0003-z

RESEARCH ARTICLE

Diana C. Roman · Katharine V. Cashman · Cynthia A. Gardner · Paul J. Wallace · John J. Donovan

Storage and interaction of compositionally heterogeneous magmas from the 1986 eruption of Augustine Volcano, Alaska

Received: 29 July 2003 / Accepted: 2 May 2005 / Published online: 26 October 2005

Abstract Compositional heterogeneity (56–64 wt% SiO_2 whole-rock) in samples of tephra and lava from the 1986 eruption of Augustine Volcano, Alaska, raises questions about the physical nature of magma storage and interaction beneath this young and frequently active volcano. To determine conditions of magma storage and evolutionary histories of compositionally distinct magmas, we investigate physical and chemical characteristics of andesitic and dacitic magmas feeding the 1986 eruption. We calculate equilibrium temperatures and oxygen fugacities from Fe-Ti oxide compositions and find a continuous range in temperature from 877 to 947°C and high oxygen fugacities (ΔNNO=1–2) for all magmas. Melt inclusions in pyroxene phenocrysts analyzed by Fourier-transform infrared spectroscopy and electron probe microanalysis are dacitic to rhyolitic and have water contents ranging from <1 to ~7 wt%. Matrix glass compositions are rhyolitic and remarkably similar (~75.9–76.6 wt% SiO_2) in all samples. All samples have ~25% phenocrysts, but lower-silica samples have much higher microlite contents than higher-silica samples. Continuous ranges in temperature and whole-rock composition, as well as linear trends in Harker diagrams and disequilibrium mineral textures, indicate that the 1986 magmas are the product of mixing between dacitic magma and a hotter, more mafic magma. The dacitic endmember is probably residual magma from the previous (1976) eruption of Augustine, and we interpret the mafic endmember to have been intruded from depth. Mixing appears to have continued as magmas ascended towards the vent. We suggest that the physical structure of the magma storage system beneath Augustine contributed to the sustained compositional heterogeneity of this eruption, which is best explained by magma storage and interaction in a vertically extensive system of interconnected dikes rather than a single coherent magma chamber and/or conduit. The typically short repose period (~10 years) between Augustine's recent eruptive pulses may also inhibit homogenization, as short repose periods and chemically heterogeneous magmas are observed at several volcanoes in the Cook Inlet region of Alaska.

Keywords Augustine · Alaska · Magma mixing · Crystallization · Andesite · Dacite · Dikes

D. C. Roman (✉) · K. V. Cashman · P. J. Wallace
Department of Geological Sciences, University of Oregon, Oregon, USA
e-mail: droman@earth.leeds.ac.uk
Tel.: +44(0)113-343-6620
Fax: +44(0)113-343-5259

C. A. Gardner
Cascades Volcano Observatory, United States Geological Survey,
Vancouver, USA

J. J. Donovan
Electron Microprobe Facility, CAMCOR, University of Oregon, Oregon, USA

Introduction

The products of an explosive volcanic eruption may be chemically homogeneous (e.g., Nye et al. 1994; Streck et al. 2002) or may span a substantial range in composition (e.g., Gourgaud et al. 1989; Coombs et al. 2000). Magma composition may vary significantly from one eruption of a particular volcano to the next (e.g., Eichelberger et al. 2000) or may be identical for eruptions that are separated by decades or even centuries (e.g., Cribb and Barton 1997). Eruptions characterized by chemically heterogeneous products may produce one homogeneous composition at the beginning and a second homogeneous composition at the end (e.g., Cioni et al. 1995; Reagan et al. 1987), or may produce magmas with a large range in composition at the beginning of an eruption that homogenize as the eruption progresses (e.g., Wolf and Eichelberger 1997). Complex combinations of the above scenarios are also observed (e.g., Hildreth and Fierstein 2000).

Understanding the conditions of magma storage, evolution, and interaction that lead to each of these scenarios has been a prime focus of petrologic study in recent years. Although several models of magma storage and interaction

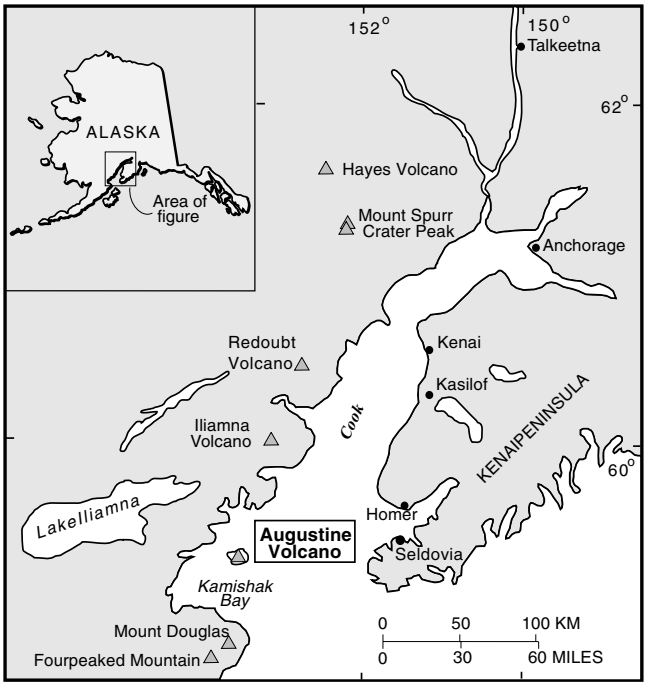

Fig. 1 Map of the Cook Inlet region showing the location of Augustine Volcano relative to other Cook Inlet region volcanoes and population centers

exist (e.g., stratified magma chambers, injection of magma into a stagnant chamber, etc.), the exact nature of magma storage and interaction is unique for each volcano, so case studies are important for testing and extending existing models. The 1986 eruption of Augustine Volcano, Alaska, presents a case in which magma remained compositionally heterogeneous throughout an episodic 6-month-long eruption. Here we examine chemical, textural, and physical properties of compositionally heterogeneous products of the early explosive phase of this eruption and present a detailed model of magma storage and interaction prior to the 1986 eruption.

Background

Augustine Volcano is a 1,200-m-high Pleistocene stratovolcano that forms an island in the eastern Aleutian arc in south-central Alaska's Cook Inlet region (Fig. 1). Augustine has erupted six times in the past 200 years (in 1812, 1883, 1935, 1964, 1976, and 1986), making it the most historically active volcano in the Cook Inlet region. Augustine erupts both explosively and effusively, with a progression from an explosive to an effusive style over a timescale of weeks to months typical of the most recent eruptions.

The 1986 eruption began explosively and ended with dome growth. Explosive activity lasted from March 27 to April 8, 1986, and produced an ash column that reached a maximum altitude of 12 km (Yount and Miller 1987). It deposited ash as far away as Anchorage, Alaska. Pyroclastic flows were also emplaced on the island during this phase. The effusive phase consisted of two episodes of dome-building. The first episode lasted from April 23–28, 1986 (Swanson and Kienle 1988), and was accompanied by the emplacement of a short, blocky lava flow high on the volcano's flanks, as well as numerous Merapi-type pyroclastic flows. The second dome-building episode, which included the extrusion of both a small dome and a Peleean-type spine, lasted from August 30–31, 1986 (Swanson and Kienle 1988). Pyroclastic flows generated during the early, explosive phase of the eruption were more pumiceous than those generated during the effusive phase. Waitt and Begét (1996) termed the deposits from these flows 'pp' (pumiceous) and 'pl' (lithic), respectively, (Fig. 2). 'Pp' deposits consist mainly of low-density pumice clasts, along with bread-crusted bombs and fine-ash particles, but also contain lithic (dense juvenile and rare non-juvenile) blocks. 'Pl' deposits consist of denser juvenile clasts and a small component of non-juvenile material. The 1986 eruption deposits contain clasts of a wide range in color and texture, as well as some banded pumice clasts. In total, the eruption produced a relatively small volume of material— the pyroclastic flow

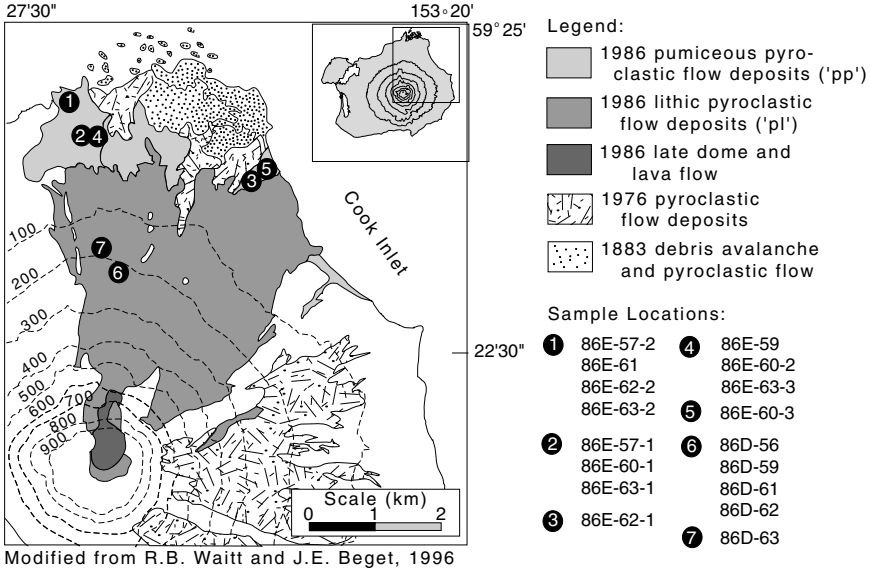

Fig. 2 Generalized geologic map of Augustine Volcano showing the location of deposits from the 1986 eruption (Waitt and Begét 1996) and locations of samples used in this study. Contour intervals in meters. *Inset map* after Waythomas and Waitt (1998)

deposits are estimated to have an expanded volume of approximately 0.05 km^3 (Swanson and Kienle 1988).

Compositional heterogeneity has been recognized in Augustine's three most recent eruptions. The compositional range present in these eruptions has been attributed to a combination of fractional crystallization (Daley 1986) and various degrees of mixing of fractionation products (Harris 1994; Johnston 1978). Johnston (1978) showed that the 1976 eruption produced a range of magma compositions from andesite to dacite (58.6–64.2 wt% SiO_2). He noted a wide compositional range (58.6–63.8 wt% SiO_2) in the early explosive phase, which appeared to narrow during the final effusive phase (62.9–64.2 wt% SiO_2). Daley (1986), however, presents an analysis of a 1976 dome sample with 56.7 wt% SiO_2, indicating the persistence of compositional heterogeneity through all stages of the 1976 eruption. Johnston (1978) suggested that mixing between a basaltic and a dacitic magma prior to the eruption produced the compositionally intermediate 1976 lavas and triggered the eruption. Harris (1994) examined products of the 1986 eruption and recognized a compositional range of 58.3–62.6 wt% SiO_2. in the effusive phases, but described the explosive phase as having only a narrow compositional range of 61.0–62.2 wt SiO_2. He argued that the 1986 lavas represent mixing between three distinct components (residual magma from the 1976 eruption, newly injected magma, and a chamber 'rind' formed by accumulation of magmas from several earlier eruptions) to produce the observed compositional heterogeneity. We were motivated to re-examine this model of magma storage by recent data (Gardner et al. 2000) indicating that the explosive phase of the 1986 eruption produced a wider compositional range (56–64 wt% SiO_2) of juvenile clasts than previously recognized.

Sample set

A sample set representing the range of colors and textures observed in the deposits of the explosive and effusive phases of the 1986 eruption was collected and analyzed for whole-rock composition by X-Ray Fluorescence at Washington State University GeoAnalytical Labs. All further analyses presented in this study are restricted to clasts from the explosive phase of the eruption as these are more likely to preserve quenched melt inclusions and Fe-Ti oxide compositions indicative of pre-ascent magma temperatures than samples from the slowly-cooled lava flow and domes. All sample names given in this paper are coded to indicate eruption phase (E = explosive or D = dome/flow) and approximate whole-rock silica content in weight percent (57–63). For a subset of nine clasts spanning the range in color, texture, and composition (56.7–63.3 wt% SiO_2) we analyzed Fe-Ti oxides by electron microprobe to determine temperature and oxygen fugacity. Additionally, we selected for melt inclusion analyses two clasts (86E-57-2, 86E-63-2) that spanned the compositional range of the eruption and were large enough to supply ample phenocrysts for Fourier-transform infrared analysis (FTIR). We also determined major element compositions of individual melt inclusions by Electron Probe Microanalysis (EPMA) (Table 3), although two of the pyroxene wafers containing the melt inclusions initially analyzed by FTIR were destroyed by the mounting process before they could be analyzed for glass composition. To expand the data set on corresponding melt inclusion volatile content and composition, we analyzed additional pyroxene and plagioclase melt inclusions in these samples (86E-57-2 and 86E-63-2) and in an additional sample of intermediate composition (86E-60-1) by EPMA, and calculated H_2O content using the 'water by difference' (WBD) method. Finally, we analyzed pyroxene compositions in three clasts (86E-57-1, 86E-57-2, and 86E-63-2) selected to represent the compositional extremes of the eruption. Sample descriptions and a summary of data types are given in Table 1, major element whole-rock compositions are given in Table 2, and sampling locations are shown in Fig. 2.

Analytical techniques

Electron probe microanalysis (EPMA)

Mineral Phases Core and rim compositions of orthopyroxene and clinopyroxene phenocrysts were analyzed by EPMA on a Cameca SX-50 at the University of Oregon under beam conditions of 15kV and 20nA, using a focused spot. Quadrilateral components were calculated from the analyses using the program QUILF (Anderson et al. 1993). Ilmenite-titanomagnetite pairs were analyzed by EPMA using beam conditions of 15 kV and 20 nA and spot sizes ranging from 1 to 5 μm. Corresponding ilmenite and magnetite grains were chosen for analysis if both were in contact with the matrix glass and were located within 200 μm of each other. Care was taken to avoid crystals that contained exsolution lamellae.

Glass Melt inclusion and matrix glasses were analyzed using beam conditions of 12 kV (melt inclusions) or 15 kV (matrix glass), 10 nA, and a spot size of 5–10 μm (analyzed melt inclusions were typically ≥100 μm in diameter). We found that the accuracy of the melt inclusion glass analyses was highly affected by the beam voltage – a beam voltage of 15 kV resulted in a large analytical volume that often included the host crystal beneath a thin inclusion, and a beam voltage of 10 kV resulted in low sensitivity for iron in the sample. Sodium migration was corrected by counting sodium in four-second increments and extrapolating the resulting count rate to time zero using the software Probe for Windows.

Fourier-transform infrared spectroscopy (FTIR)

Pyroxene-hosted melt inclusions were analyzed for H_2O and CO_2 by FTIR. Although plagioclase is the dominant phase in all samples, plagioclase-hosted melt inclusions are generally small (<10 μm in diameter), making them unsuitable for FTIR analysis. Furthermore, they frequently preserve glasses with evolved compositions and low water contents (e.g., Coombs et al. 2000; Roman 2001) similar

Table 1 Sample set, description, and subsets analyzed for whole-rock composition, temperature/oxygen fugacity, volatile content by FTIR, volatile content and composition of melt inclusions and matrix glasses by EPMA, and pyroxene composition

Field name	Sample name	Description	Phase	WR XRF	Fe-Ti oxides	FTIR	Glass EPMA	Px
990815-8	86E-57-1	Black dense	E	X	X			X
A0186-1	86E-57-2	Med gray pumice	E	X		X	X	X
980722-2	86E-59	Black scoria	E	X	X			
990815-9	86E-60-1	Lt. med. gray Pumice	E	X	X		X	
980722-4	86E-60-2	Med. gray pumice	E	X	X			
980722-8	86E-60-3	Med. gray pumice	E	X	X			
990815-6	86E-61	Med. gray pumice	E	X	X			
990818-14	86E-62-1	Lt. gray pumice	E	X	X			
990815-5	86E-62-2	Lt. gray Pumice	E	X	X			
990815-10	86E-63-1	Lt. gray pumice	E	X	X			
A0186-2	86E-63-2	Lt. gray pumice	E	X		X	X	X
980722-5	86E-63-3	Lt. gray pumice	E	X	X			
990816-12	86D-56	Black	D	X				
990816-7	86D-59	Gray	D	X				
990816-13	86D-61	Gray	D	X				
990816-9	86D-62	Gray	D	X				
990816-6	86D-63	Gray	D	X				

E – explosive phase, D – dome building/lava flow phase

to the matrix glass and presumably not indicative of deeper storage conditions. We were careful to select for FTIR analysis only melt inclusions that were glassy and contained no large bubbles, although some included a small oxide crystal.

Sample preparation techniques and analytical conditions for FTIR analysis are described in detail by Wallace et al. (1999). Samples were crushed and sieved, and pyroxene phenocrysts were separated by hand under a binocular microscope and cleaned in a bath of HBF_4 to remove all adhering glass. Pyroxene phenocrysts were mounted in acetone-soluble adhesive and polished on both sides. In most cases, the melt inclusion of interest was intersected only on one side of the pyroxene wafer. Transmission infrared spectra of the melt inclusions were obtained using the University of Oregon's Thermo Nicolet Nexus 670 Fourier-Transform Infrared Spectrometer (FTIR) interfaced with a Continuum IR microscope. The FTIR has a globar source, an extended KBr beamsplitter, and a liquid nitrogen-cooled MCT-A detector. The infrared beam was directed through an adjustable aperture and manually focused on the melt inclusion.

Band assignments for water and carbon dioxide dissolved in rhyolitic glass are taken from Newman et al. (1986) and Newman et al. (1988), respectively. Water is present as molecular H_2O at 5,200 cm^{-1} and 1,630 cm^{-1}, as OH^- at 4,500 cm^{-1}, and as total H_2O at 3,550 cm^{-1}. Molecular CO_2 is present at 2,350 cm^{-1}. A reference spectrum was

Table 2 Representative major element whole-rock compositions (measured by XRF) of 1986 eruption samples (normalized to 100%)

Sample	SiO_2	Al_2O_3	TiO_2	FeO[a]	MnO	CaO	MgO	K_2O	Na_2O	P_2O_5	Orig. total
86E-57-1	56.7	17.3	0.75	6.82	0.14	8.72	5.12	0.72	3.54	0.13	100.3
86E-57-2	57.3	17.6	0.71	6.64	0.14	8.63	4.79	0.73	3.34	0.12	100.1
86E-59	59.3	17.4	0.66	5.64	0.13	8.01	4.21	0.83	3.66	0.14	98.3
86E-60-1	60.2	16.8	0.63	6.01	0.13	7.40	4.11	0.90	3.65	0.13	99.6
86E-60-2	60.3	17.2	0.63	5.48	0.13	7.59	3.95	0.89	3.77	0.14	98.9
86E-60-3	60.4	17.0	0.64	5.55	0.13	7.54	4.07	0.88	3.73	0.14	99.7
86E-61	60.7	17.0	0.61	5.73	0.13	7.27	3.74	0.93	3.81	0.13	99.8
86E-62-1	61.7	16.6	0.59	5.51	0.13	6.97	3.64	0.96	3.73	0.14	99.5
86E-62-2	62.3	16.6	0.58	5.41	0.13	6.65	3.41	1.02	3.79	0.14	99.7
86E-63-1	62.8	16.4	0.57	5.39	0.13	6.44	3.34	1.05	3.82	0.14	99.1
86E-63-2	62.8	16.7	0.55	5.23	0.12	6.56	3.21	1.03	3.73	0.13	99.7
86E-63-3	63.2	16.5	0.57	4.85	0.12	6.45	3.21	1.05	3.94	0.15	99.7
86D-56	56.8	17.3	0.74	6.81	0.15	8.83	5.18	0.72	3.31	0.14	98.3
86D-59	58.7	17.0	0.68	6.42	0.14	8.00	4.58	0.82	3.58	0.13	100.3
86D-61	61.5	16.7	0.61	5.48	0.13	7.10	3.69	0.97	3.70	0.14	98.6
86D-62	61.8	16.8	0.60	5.67	0.12	6.83	3.47	0.83	3.70	0.14	99.9
86D-63	62.6	16.9	0.54	5.13	0.12	6.56	3.14	1.02	3.92	0.13	100.0

[a]Total iron is expressed as FeO in all tables

Table 3 Major-element compositions (by EPMA) and H_2O contents (determined using the WBD method - see text for discussion) of melt inclusions analyzed by FTIR. Reported analyses are average of three individual analyses

Sample/inclusion number	SiO_2	Al_2O_3	TiO_2	FeO	CaO	MgO	K_2O	Na_2O	Cl	SO_3	H_2O (WBD)
86E-63-2/3-1	73.82	12.59	0.23	1.56	2.05	0.15	1.70	3.82	0.27	0.04	3.77
86E-63-2/3-2	73.26	13.23	0.22	1.48	2.03	0.14	1.62	4.02	0.22	0.04	3.74
86E-63-2/5-1	71.11	12.66	0.35	2.07	2.35	0.17	1.65	3.65	0.26	0.02	5.71
86E-63-2/6-1	72.92	12.19	0.13	1.77	2.11	0.14	1.73	3.51	0.28	0.04	5.18
86E-63-2/8-1	74.60	12.05	0.34	2.34	1.94	0.27	2.18	4.27	0.37	0.05	1.59
86E-63-2/8-3	72.02	12.71	0.27	1.80	2.17	0.14	1.93	3.62	0.34	0.04	4.97

obtained for pyroxene and subtracted from all spectra for melt inclusions that are intersected on one side only to remove peaks due to the pyroxene host. Peak heights were measured using Omnic software in all cases where the peak could be distinguished from noise. As most of the melt inclusions analyzed in this study were relatively thin, many absorption peaks (especially that for CO_2) could not be distinguished from spectral noise. For all but one of the melt inclusions in sample 86E-57-2, water species peaks were too small to be distinguished from noise, and only the height of the total water peak (at 3,550 cm^{-1}) was measured.

Total amounts of dissolved H_2O and CO_2 were calculated from peak heights using Beer's law:

$$c = \frac{(\mathrm{mw})\,(\mathrm{abs})}{\rho \mathrm{d}\varepsilon} \quad (1)$$

where c is the concentration of the species, mw is the molecular weight of the species, abs is the absorbance or peak height, ρ is the density of the glass, d is the thickness of the inclusion, and ε is the molar absorption coefficient. Glass densities were calculated from the composition of the melt inclusions following Ochs and Lange (1999), using iterative water contents beginning with 0 wt% (i.e., the first calculation of total water was made based on an anhydrous density, then density was recalculated using the resulting water content and water content was recalculated once using the hydrous density). Inclusion thicknesses were measured by mounting each pyroxene wafer on the tip of a needle, immersing it in refractive index oil, and orienting it so that the inclusion could be viewed in cross-section under a binocular microscope. Thickness was read from the calibrated scale bar on the microscope's eyepiece, and is considered accurate to within ±5 μm. Molar absorption coefficients are taken from Newman et al. (1986) for water species and Blank et al. (1993) for CO_2. The accuracy of the results from FTIR analysis is limited primarily by the accuracy of peak height (which decreases with decreasing inclusion thickness) and inclusion thickness measurements.

Calibration of the water-by-difference (WBD) method

For melt inclusions not analyzed by FTIR, we estimated H_2O using the simple WBD method based on EPMA analyses. Because other variables, such as errors in the calibration of the microprobe and matrix corrections, or the presence of significant amounts of unmeasured elements in the melt inclusion glass, may also affect microprobe analysis totals, we used our FTIR results to check the accuracy of this method (e.g., Devine et al. 1995).

EPMA requires that measured x-ray intensities must be corrected for the specimen matrix effects (absorption, fluorescence and backscatter/energy loss) of all elements contained in the sample (e.g., Tingle et al. 1996). Analytical accuracy is typically confirmed by obtaining totals approaching 100%. In the characterization of hydrous glasses, however, oxygen is calculated by stoichiometry and hydrogen in the matrix cannot be measured by EPMA, thus it has been routine to calculate matrix corrections without including the hydrous component. In some cases, however, this "missing" water can have a substantial effect on the matrix correction and thus the calculated composition of the glass. This in turn has an effect on WBD values, which are calculated by subtracting the analysis total from 100%. For hydrous rhyolitic glasses, the addition of water into the matrix calculation increases the absorption correction for all other components in the sample, especially for the more highly absorbed low energy x-rays (e.g., Si kα and Al kα, the former of which comprises most of the matrix). To correct for matrix effects introduced by the presence of H_2O, the EPMA software package Probe for Windows recalculates all melt inclusion compositions by iteratively adjusting water content and recalculating until the analysis totals 100% (Donovan and Tingle 1996). Although this technique results in only a small increase in the concentration of the individual cations, collectively it can result in ∼1 wt% absolute decrease in the calculated WBD.

We plot total water content of melt inclusions measured directly by FTIR vs. water content of melt inclusions estimated using the WBD method (Table 3) in Fig. 3, showing WBD estimates both before and after the iterative hydrous matrix correction. Before matrix correction, the WBD method consistently overestimates melt inclusion water content by approximately 1 wt%. Iteratively matrix-corrected WBD estimates are more accurate, with an error of less than 0.5 wt%. A linear regression through the corrected points and fixed at the origin has an approximately 1:1 slope and an R^2 value of 0.73. This indicates that careful analysis of melt inclusions by EPMA may be used to reliably estimate melt inclusion water content using the methods, analytical conditions, and analysis corrections outlined here.

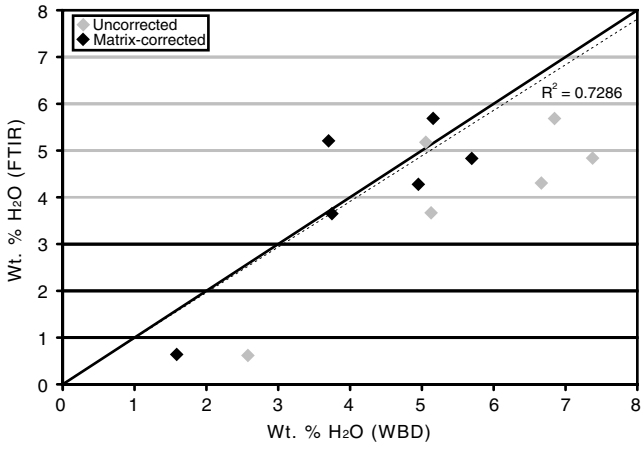

Fig. 3 Comparison of melt inclusion water contents measured by FTIR in sample 86E-63-2 (Table 6) to melt inclusion water contents estimated as the difference between 100% and microprobe analysis totals (the 'water-by-difference' method – Table 3). *Solid diagonal line* indicates 1:1 correspondence,*dashed line* is a linear regression fixed at the origin. *Gray diamonds* show WBD water content before matrix correction of the analysis and *black diamonds* show matrix-corrected WBD estimates.

Results

Whole-rock compositions and mineralogy

Whole-rock analyses obtained as part of this study (Table 2) indicate that the compositional ranges of both the explosive and effusive phases of the 1986 eruption are wider than previously thought. Both phases produced basaltic andesite through dacite with approximately 57–63 wt% SiO_2 (Table 2), similar to compositional ranges observed in the products of the 1976 eruption of Augustine and in the products of other recent eastern Aleutian eruptions including the 1953–1974 eruption of Southwest Trident (56–65 wt% SiO_2, Coombs et al. 2000), the andesite-dacite portion of the 1912 Katmai eruption (58–66 wt% SiO_2, Hildreth 1983), and the 1990 eruption of Redoubt Volcano (58–63 wt% SiO_2, Nye et al. 1994). Major-element Harker diagrams of explosive and effusive phase whole-rock compositions show compositional continuity and linear trends in all cases (Fig. 4).

Plagioclase is the dominant mineral phase in all clasts, with lesser clinopyroxene, orthopyroxene, magnetite, and ilmenite in all samples. Minor olivine is present in some samples (Harris 1994). The occurrence of hornblende is limited to a few small phenocrysts showing extensive textural disequilibrium (Harris 1994).

Temperature and oxygen fugacity

Equilibrium temperatures of Augustine magmas were determined using the two-oxide geothermometer of Anderson and Lindsley (1988). First, all Fe-Ti oxide compositions were subjected to the Mg-Mn equilibrium test of Bacon and Hirschmann (1988). Any oxide pair that did not plot within the analytical error bounds of this equilibrium line was rejected. Remaining oxide compositions were entered into the program QUILF (Anderson et al. 1993) to obtain equilibrium temperatures and oxygen fugacities. Average temperatures, oxygen fugacities, and standard deviations are given in Table 4.

Table 4 Number of ilmenite-magnetite pairs, average temperatures, oxygen fugacities, and standard deviations for all explosive phase (pp) samples containing both Fe-Ti oxides.

Sample	# of analyses	Average Temp°C	Temp. SD[a]	Average $f(O_2)$	$f(O_2)$ SD[a]
86E-57-1	15	947	40	-10.04	0.51
86E-59	4	943	10	-9.51	0.13
86E-60-1	7	923	25	-9.88	0.30
86E-60-2	3	920	10	-9.93	0.11
86E-60-3	4	902	16	-10.05	0.19
86E-61	4	890	24	-10.14	0.42
86E-62-1	12	877	20	-10.47	0.33
86E-62-2	5	880	21	-10.46	0.52
86E-63-1	5	880	9	-10.34	0.15
86E-63-3	8	886	18	-10.29	0.29

[a]SD: standard deviation

Fe-Ti oxide geothermometry indicates that the 1986 magmas ranged in temperature from 877 to 947°C. Variations in temperature and oxygen fugacity in the sample set are generally related to whole-rock composition (Fig. 5), with a general decrease in temperature for samples in the compositional range 59.3–62.6 wt% SiO_2 (whole-rock); higher-silica samples being cooler than lower-silica samples. Temperatures of 877–890°C for samples with 60.7–63.3 wt% SiO_2 are similar to temperatures of 867–885°C calculated for two 1976 samples with 62.1–62.3 wt% SiO_2 (Harris 1994). Calculations also indicate a range in oxygen fugacity for the 1986 magmas. A plot of log $f(O_2)$ versus temperature for analyzed samples shows that relative oxygen fugacities range from ΔNNO of +1 to +2 (Fig. 6). Most samples are generally more oxidized (NNO+2) and similar to magmas from the 1976 eruption (Harris 1994), whereas the hottest and most mafic sample (86E-57-1) has a lower oxygen fugacity of NNO+1.

Pyroxene

Augite (cpx) and orthopyroxene (opx) are found in all samples from the 1986 eruption. Analyses of pyroxene phenocryst cores and rims are listed in Table 5 and shown in Fig. 7. Harris (1994) noted that the range of opx and cpx composition is limited in both the 1986 and 1976 eruptions, but examined only data from samples with 58.3–62.2 wt% whole-rock SiO_2. Although we find only unzoned pyroxene in our dacitic sample, we observed reversely zoned cpx and opx in samples with $SiO_2 < 58$ wt%.

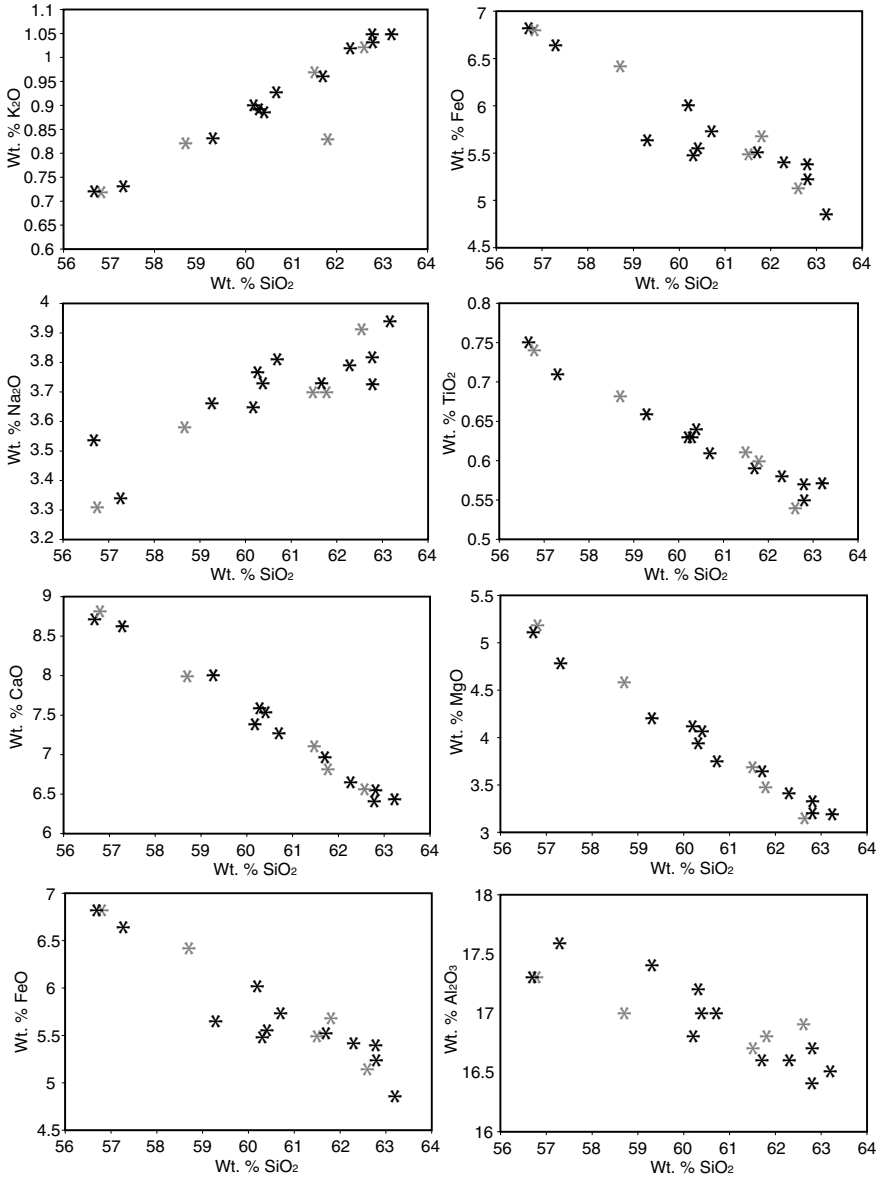

Fig. 4 Major-element Harker diagrams of whole-rock compositions of samples from the 1986 eruption. *Black asterisks* indicate 'pp' samples (from the explosive phase) and *gray asterisks* indicate 'pl' samples (from the effusive phase)

Volatile content and composition of melt inclusion glasses

Pyroxene-hosted melt inclusions in two samples (86E-57-2 and 86E-63-2) representing endmember whole-rock compositions were analyzed for volatile (H_2O and CO_2) contents by FTIR (Table 6). Maximum melt inclusion water contents measured by FTIR are 2.6 and 5.7 wt% in the two samples, respectively, and maximum measured CO_2 concentrations are 34 and 177 ppm.

All of the analyzed melt inclusions, regardless of whole-rock composition or water content, are dacitic to rhyolitic (~69.8–77.2 wt% SiO_2 on an anhydrous basis, Tables 3 and 7) and significantly more evolved than whole-rock compositions (Table 2). Melt inclusion water contents estimated using the WBD method range from < 1 wt% to > 5 wt% in all samples, and as high as 7 wt% in the most silicic sample (Table 7). The Cl contents of melt inclusions from the high-silica sample (86E-63-2) were also analyzed by EPMA (Table 3). Dissolved Cl is relatively high (0.22–0.37 wt%) in all melt inclusions and increases slightly with decreasing H_2O. The variation of Cl in Augustine melt inclusions as a function of equilibrium pressure (determined from measured H_2O and CO_2) is similar to that observed in experiments and provides strong evidence for saturation of the magmas with both H_2O-CO_2-Cl vapor and an alkali-chloride-rich hydrosaline melt during magma decompression (e.g., Metrich and Rutherford 1992; Lowenstern 1994).

Matrix glasses

Matrix glasses (Table 8) are high-silica rhyolite (75.9–76.6 wt% SiO_2 on an anhydrous basis) in all three samples, regardless of whole-rock composition. H_2O contents of matrix glasses estimated using the WBD method range from 0.76 to 1.18 wt%.

Table 5 Major-element compositions of ortho- and clinopyroxene cores and rims (normalized to 100%), quadrilateral components, and Mg number. Each line represents a single analysis, and each core and rim pair represents one phenocryst

Sample		SiO_2	Al_2O_3	TiO_2	FeO	MnO	MgO	Cr_2O_3	CaO	Na_2O	Original total	WO	EN	FS	Mg #
86E-57-2 Cpx 1	Core	52.33	1.54	0.28	9.02	0.39	14.39	0.00	21.69	0.35	98.95	42.51	44.65	12.83	73.98
	Rim	52.49	1.56	0.27	8.77	0.28	14.75	0.00	21.57	0.32	99.09	42.14	45.26	12.60	74.99
86E-57-2 Cpx 2	Core	52.63	1.48	0.26	8.90	0.38	14.58	0.00	21.46	0.31	99.41	42.33	44.27	13.40	74.49
	Rim	48.39	6.89	1.15	7.22	0.15	13.90	0.06	21.96	0.28	99.45	36.91	53.32	9.77	77.43
86E-57-2 Cpx 3	Core	52.54	1.35	0.23	9.16	0.40	14.46	0.00	21.49	0.36	99.10	42.42	44.39	13.18	73.78
	Rim	52.09	1.63	0.33	9.01	0.39	14.63	0.07	21.52	0.33	99.14	41.68	45.96	12.36	74.31
86E-57-2 Cpx 4	Core	52.49	1.53	0.32	9.15	0.36	14.81	0.00	21.00	0.34	99.32	41.34	45.26	13.39	74.26
	Rim	50.25	4.98	0.71	7.35	0.16	14.70	0.05	21.48	0.31	99.53	38.19	51.29	10.58	78.18
86E-57-2 Cpx 5	Core	51.95	1.88	0.38	9.37	0.40	14.39	0.00	21.25	0.37	98.93	41.33	45.44	13.23	73.25
	Rim	52.93	1.08	0.24	8.16	0.40	15.04	0.00	21.84	0.31	98.56	43.18	45.22	11.60	76.67
86E-57-2 Opx 1	Core	53.16	0.71	0.12	20.40	0.83	23.86	0.02	0.90	0.00	98.16	1.86	67.66	30.48	67.58
	Rim	53.32	0.82	0.16	20.18	0.81	23.59	0.02	1.06	0.03	98.48	2.19	66.78	31.03	67.57
86E-57-2 Opx 2	Core	53.35	1.95	0.12	17.12	1.44	25.96	0.00	0.04	0.02	99.28	0.08	74.21	25.71	72.99
	Rim	54.07	1.58	0.12	16.67	1.33	26.16	0.01	0.04	0.02	98.94	0.08	73.63	26.29	73.67
86E-57-2 Opx 3	Core	53.08	1.15	0.20	20.04	0.61	23.72	0.00	1.19	0.01	98.91	2.47	67.09	30.44	67.85
	Rim	53.40	0.80	0.16	20.06	0.79	23.69	0.04	1.06	0.01	98.84	2.18	66.84	30.98	67.80
86E-57-1 Cpx 1	Core	52.65	1.50	0.30	8.91	0.35	14.49	0.03	21.41	0.36	99.54	42.57	43.93	13.51	74.35
	Rim	49.66	5.33	0.90	7.24	0.15	14.50	0.13	21.83	0.27	100.13	38.20	51.82	9.98	78.12
86E-57-1 Cpx 2	Core	52.75	1.45	0.25	9.05	0.34	14.44	0.00	21.40	0.32	100.46	42.53	43.43	14.04	73.99
	Rim	50.00	4.65	0.85	8.97	0.21	14.34	0.00	20.67	0.30	100.17	37.17	49.46	13.37	74.03
86E-57-1 Opx/Cpx 1	Core	53.43	0.96	0.17	20.37	0.71	23.29	0.00	1.07	0.01	99.54	2.19	65.61	32.20	67.08
	Rim	51.99	2.45	0.47	8.60	0.26	14.98	0.01	20.95	0.29	99.74	40.21	46.76	13.03	75.64
86E-57-1 Opx/Cpx 2	Core	53.61	0.84	0.15	19.94	0.75	23.54	0.02	1.16	0.01	99.67	2.37	66.18	31.45	67.79
	Rim	47.47	7.88	1.38	7.08	0.12	13.36	0.11	22.30	0.30	99.34	36.70	53.98	9.32	77.09
86E-57-1 Opx 1	Core	54.86	0.56	0.14	19.92	0.71	22.62	0.01	1.16	0.01	98.32	2.41	65.32	32.27	66.93
	Rim	54.80	0.58	0.14	19.95	0.69	22.63	0.00	1.19	0.01	97.34	2.47	65.25	32.28	66.91
86E-57-1 Opx 2	Core	54.00	0.63	0.15	19.94	0.83	23.44	0.00	1.00	0.00	100.37	2.04	66.31	31.65	67.69
	Rim	53.85	1.72	0.34	16.85	0.47	24.89	0.02	1.80	0.06	99.38	3.69	69.8	26.51	72.47
86E-63-2 Cpx 1	Core	52.48	1.46	0.26	9.00	0.36	14.66	0.04	21.41	0.34	98.78	41.99	45.09	12.92	74.39
	Rim	52.22	1.73	0.34	9.01	0.34	14.60	0.00	21.41	0.35	98.30	41.76	45.44	12.80	74.29
86E-63-2 Cpx 2	Core	51.83	1.92	0.40	9.12	0.34	14.63	0.00	21.38	0.38	98.85	41.20	46.69	12.11	74.10
	Rim	52.57	1.20	0.22	8.41	0.41	14.93	0.00	21.93	0.33	98.79	42.77	46.13	11.11	75.98
86E-63-2 Cpx 3	Core	52.29	1.57	0.26	8.77	0.43	14.53	0.07	21.71	0.38	98.94	42.33	45.60	12.06	74.69
	Rim	52.56	1.38	0.24	8.82	0.38	14.66	0.00	21.61	0.34	99.07	42.46	44.99	12.55	74.77
86E-63-2 Opx 1	Core	53.07	0.94	0.15	20.08	0.68	23.80	0.00	1.27	0.01	98.90	2.64	67.45	29.91	67.88
	Rim	53.84	0.47	0.11	19.72	0.89	23.86	0.01	1.10	0.00	98.50	2.23	66.88	30.89	68.32
86E-63-2 Opx 2	Core	53.32	0.83	0.17	19.89	0.78	23.93	0.04	1.04	0.00	98.33	2.14	67.55	30.31	68.19
	Rim	53.37	0.79	0.16	19.90	0.78	23.91	0.00	1.07	0.02	98.49	2.21	67.54	30.26	68.17
86E-63-2 Opx 3	Core	53.14	0.78	0.13	20.42	0.87	23.74	0.01	0.90	0.00	98.27	1.87	67.38	30.75	67.45
	Rim	53.14	0.96	0.18	20.14	0.63	23.79	0.02	1.13	0.01	98.27	2.34	67.25	30.41	67.80

Discussion

Origin of compositionally heterogeneous magmas

Based on the results of least-square modeling of phenocryst and groundmass glass compositions of samples from the effusive phase of the 1986 eruption, Harris (1994) argued that the compositional range present in the 1986 eruption resulted from mixing of a basaltic and a silicic magma prior to the onset of eruption, as opposed to simple crystal fractionation. He also noted resorbed olivine in samples with <62 wt% SiO_2 from the 1986 eruption, providing additional evidence for mixing prior to the eruption. Our analyses of compositionally variable samples from the explosive phase of the 1986 eruption support the general model of mafic injection and mixing proposed by Harris (1994). Harker diagrams of explosive and effusive phase compositions (Fig. 3) show linear trends indicative of mixing between two compositionally distinct parent magmas, suggesting a common storage system. The observed continuous ranges in temperature and oxygen fugacity (Figs. 5 and 6) indicate post-mixing re-equilibration or crystallization of Fe-Ti oxides in all

Table 6 H_2O and CO_2 content of melt inclusions measured by FTIR spectroscopy. Total water is calculated directly from the height of the 3550 cm^{-1} peak for sample 86E-57-2, and as the average of the two molecular H_2O determinations plus the amount of OH- for sample 86E-63-2 (in which thicker melt inclusions allowed for accurate measurement of these peak heights)

Sample number	Inclusion number 5200	Inclusion thickness (μm)	Absorbance/b and(cm^{-1}) 4500	3550	2350	1630		Total H_2O (wt%)	CO_2 (ppm)
86E-57-2	5-3	25			0.105			0.88	n.m.[a]
86E-57-2	5-4	25			0.31	0.005		2.62	34
86E-63-2	3-1	42	0.0179	0.0116		0.026	0.827	3.64	108
86E-63-2	3-2	39	0.0295	0.0111		0.0202	1.155	5.17	91
86E-63-2	5-1	26	0.019	0.0043		0.0258	0.843	4.81	175
86E-63-2	6-1	31	0.0278	0.0075		0.031	1.041	5.66	177
86E-63-2	8-1	61	0.0014	0.0051		0.0063	0.159	0.60	18
86E-63-2	8-3	28	0.0186	0.0067		0.0267	0.632	4.28	168

[a]n.m. – not measured (inclusion was too thin to produce a measurable peak)

Table 7 EPMA analyses of melt inclusions and H_2O contents by WBD

Sample	SiO_2	Al_2O_3	TiO_2	FeO	CaO	MgO	K_2O	Na_2O	H_2O
86E-57-2	72.86	11.68	0.60	2.63	1.97	0.73	1.33	4.25	3.94
86E-57-2	71.72	12.41	0.67	3.12	2.47	0.58	1.70	4.25	3.08
86E-57-2	69.60	12.02	0.79	2.75	3.71	1.44	1.30	4.58	3.80
86E-57-2*	74.29	11.61	0.65	3.14	1.83	0.62	3.05	4.82	0.00
86E-57-2	68.92	13.75	1.07	3.27	3.26	0.98	1.42	4.38	2.96
86E-57-2	69.89	13.57	0.89	2.73	2.91	0.80	1.84	4.23	4.12
86E-57-2[a]	72.00	13.35	0.82	2.94	2.45	0.35	2.26	4.74	1.09
86E-57-2[a]	75.02	11.52	1.00	2.23	1.38	0.33	2.37	4.68	1.47
86E-57-2	69.38	14.82	0.75	2.72	3.43	0.62	2.18	5.42	0.65
86E-57-2	68.61	13.80	0.72	3.09	3.45	1.33	1.46	3.18	4.35
86E-57-2	72.84	11.27	0.06	4.11	1.72	2.25	2.31	3.20	2.24
86E-57-2	71.49	11.71	0.83	3.43	1.36	1.91	2.59	4.28	2.40
86E-57-2	72.68	12.13	1.08	3.36	2.26	0.30	1.77	4.37	2.05
86E-57-2	70.37	11.62	1.19	3.14	1.46	0.36	2.28	4.25	5.33
86E-57-2	68.66	13.70	0.77	2.74	3.56	0.93	1.24	4.15	4.26
86E-57-2	72.70	12.21	0.73	3.45	1.83	0.31	2.48	4.28	2.01
86E-57-2	70.93	12.42	0.45	3.11	2.01	0.36	2.03	4.00	4.68
86E-57-2	71.02	13.58	0.31	3.68	1.71	0.51	2.74	5.80	0.65
86E-60-1[a]	71.24	12.71	0.48	2.53	2.29	0.32	1.73	4.89	3.82
86E-60-1	70.25	12.58	0.33	2.15	2.30	0.71	1.78	3.94	5.95
86E-60-1	71.70	12.55	0.50	3.91	1.19	0.28	3.27	4.99	1.62
86E-60-1	72.35	12.19	0.61	2.97	0.64	0.42	3.24	4.45	3.13
86E-60-1	70.69	13.17	0.39	2.22	2.03	0.21	2.34	4.38	4.58
86E-60-1	71.06	12.93	0.48	3.30	1.19	0.43	3.12	4.99	2.50
86E-60-1	73.90	12.67	0.25	2.76	1.13	0.58	3.23	4.89	0.58
86E-60-1	69.79	13.09	1.07	1.48	2.79	0.66	1.48	4.40	5.23
86E-60-1	72.74	13.04	0.22	2.63	1.64	0.21	2.69	5.26	1.57
86E-60-1	69.68	13.04	0.69	2.18	2.21	0.43	1.61	3.83	6.33
86E-63-2	73.07	14.36	0.39	0.78	3.14	0.25	2.14	4.26	1.62
86E-63-2	69.04	14.58	0.41	0.58	2.34	0.14	1.82	3.93	7.17
86E-63-2	71.69	13.98	0.44	3.10	2.68	0.30	1.97	4.33	1.50
86E-63-2[a]	72.65	12.60	0.56	1.25	1.74	0.07	2.25	4.25	4.81

[a]Inclusion in plagioclase

Table 8 Matrix glass compositions analyzed by EPMA, including H_2O determined using the WBD method

Sample	Analyses	SiO_2	Al_2O_3	TiO_2	FeO	CaO	MgO	K_2O	Na_2O	H_2O
86E-57-2	5	75.80	12.62	0.35	1.69	1.66	0.38	2.23	4.23	1.04
86E-60-1	5	75.14	12.14	0.70	2.53	1.63	0.73	2.34	4.11	1.18
86E-63-2	7	75.33	11.59	0.75	2.66	1.79	0.63	2.58	3.92	0.76

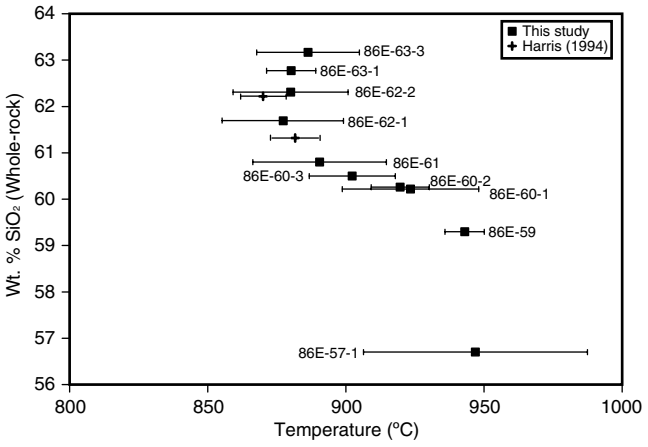

Fig. 5 Plot of SiO_2 content vs. temperature range. The average temperature for a sample is shown by the *square*; *error bars* indicate one standard deviation. *Temperature ranges with plus symbols* indicate temperatures calculated from data presented by Harris (1994)

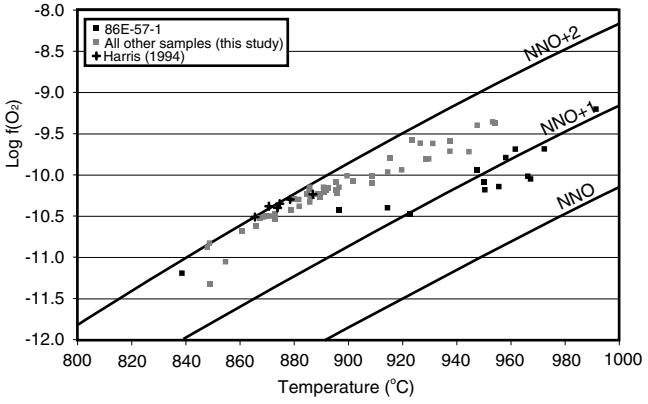

Fig. 6 Plot of log $f(O_2)$ vs. temperature for all data. *Black squares* indicate data for the most mafic sample 86E-57-1. *Gray squares* indicate data from all other samples in this study. *Plus symbols* indicate data calculated from analyses of 1976 and 1986 explosive phase samples presented by Harris (1994) Equation for the NNO buffer is taken from Huebner and Sato (1970)

1986 magmas, which may occur on timescales of days to weeks (Venezky and Rutherford 1999).

One of the most unique aspects of the 1986 eruption of Augustine is that it produced a compositionally variable suite of magmas through the entire course of the eruption. It is far more common for a mixing event to produce a homogeneous magma that retains traces (e.g., mafic enclaves, disequilibrium mineral assemblages or textures) of the compositionally distinct parent magmas (e.g., Venezky and Rutherford 1999), or to result in progressive homogenization through the eruption (e.g., Wolf and Eichelberger 1997). In the case of Augustine, it appears that significant amounts of at least one mixing endmember erupted in all phases of the 1986 eruption. One of the mixing endmembers for the 1986 eruption is probably represented by the most silicic ($\geq$ 62 wt% SiO_2) clasts, which preserve no evidence of disequilibrium textures, reverse pyroxene zoning, or bimodal phenocryst core compositions, all of which would be expected if some phases were inherited from a

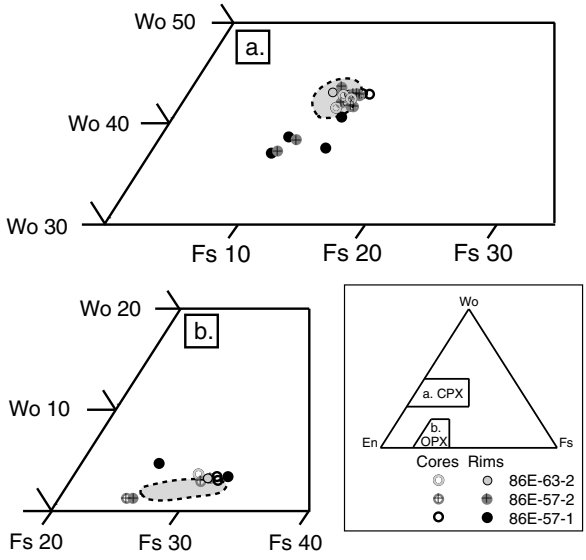

Fig. 7 Core and rim compositions of pyroxene phenocrysts in one high-silica sample (86E-63-2) and two low-silica samples (86E-57-2 and 86E-57-1) of the 1986 eruption. *Gray shaded* areas denote ranges of cpx and opx core and rim compositions analyzed by Harris (1994) and Johnston (1978)

compositionally distinct parent. It is likely that this silicic endmember is residual magma from the 1976 eruption, the end of which appears to have been dominated by dacitic magma of similar composition (62.9–64.2 wt% SiO_2, Johnston 1978) and temperature (876°C, Harris 1994). It is not clear from our analyses whether our hottest and most mafic sample (86E-57-1), which is distinct from all others in its lower oxygen fugacity (NNO+1), represents the mafic endmember to mixing. Although we found no evidence of a more mafic endmember (e.g., basaltic enclaves) in our samples of the 1986 eruption, we note that basaltic lavas (51.5 wt% SiO_2) have been found at Augustine in the deposits of earlier eruptions (Daley 1986).

Model of the magma storage system

Preserved compositional heterogeneity requires a physical barrier to homogenization that existed through the course of the 1986 eruption. While it is possible that differences in the physical properties (e.g., viscosity) of the parent magmas inhibited mixing, the significant body of evidence for partial or complete homogenization of parent mafic and dacite magmas (e.g., Wolf and Eichelberger 1997, Gourgaud et al. 1989) leads us to conclude that this was not the main barrier to homogenization. Rather, we argue that the structure of the magma storage and transport system beneath Augustine inhibited mixing prior to and during the 1986 eruption.

We propose that magmas feeding the 1986 eruption were stored in a system of interconnected dikes (Fig. 8). In this model, the system of dikes was occupied initially by cooler, dacitic magma left over from the 1976 eruption. A hotter and more mafic magma then began to intrude sections of the network, ultimately destabilizing the system and initiating the onset of eruption. Some of the dikes storing

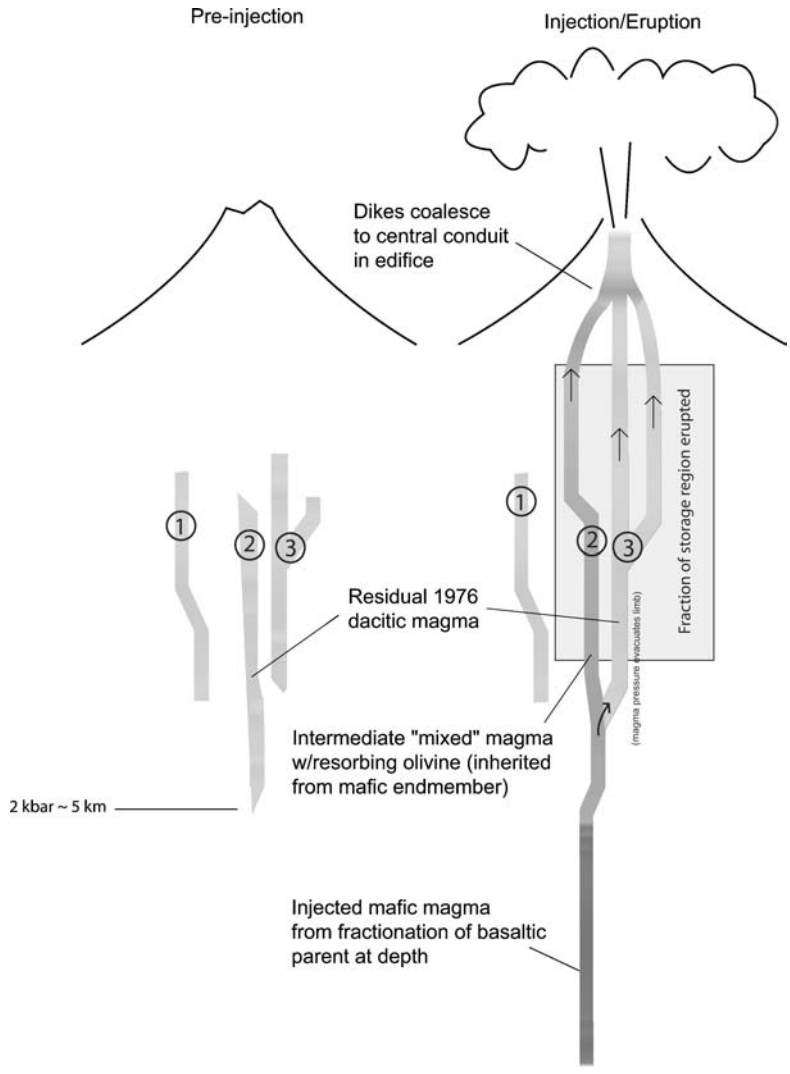

Fig. 8 Schematic of magma storage and interaction prior to and during the 1986 eruption. *Numbers* show three possible scenarios for magma migration and interaction: 1. A pre-existing dike that is not intruded by new magma and whose contents are not erupted, 2. A pre-existing dike intruded by mafic magma to form an intermediate magma, which is erupted, and 3. a pre-existing dike intruded by mafic magma, which forces out the non-mixed magma occupying the dike before intrusion

residual 1976 magmas received inputs of mafic magma, which mixed readily to produce magmas with intermediate compositions, temperatures, and disequilibrium mineral textures (e.g., resorbed olivine), and zoned pyroxene phenocrysts. Other dikes storing residual magmas fed the eruption but did not receive inputs of new magma. This model explains both the presence of significant amounts of the silicic endmember magma in the eruption, as well as the persistence of compositional heterogeneity in the later phases of the eruption. It is also consistent with the short repose interval (10 years) between consecutive eruptions, as longer repose intervals might allow residual magmas to cool and solidify. We surmise that the dike system may have extended over depths of 4–5 km below the summit of Augustine, based on the maximum melt inclusion water contents indicating maximum storage pressures of ~200 MPa and the location of earthquake clusters at this depth prior to and during the 1976 eruption (Kienle 1987; seismicity was not observed at this depth prior to the 1986 eruption, probably due to changes the configuration of the local seismic network between 1976 and 1986 (Power 1988)).

Melt inclusions as a record of magma evolution

We are interested in understanding the origin of analyzed melt inclusions and host phenocrysts, as these melt inclusions may preserve additional information on pre-ascent melt compositions and magma mingling and mixing. A Harker diagram (K_2O vs. SiO_2) for whole-rock, melt inclusion, and matrix glass analyses (Fig. 9) shows a wide range in potassium contents for melt inclusion analyses, particularly for the low- (86E-57-2) and intermediate-silica (86E-60-1) samples. This suggests a complex history of melt inclusion entrapment for these two samples.

Origin of high-H_2O melt inclusions and host phenocrysts

Melt inclusions with high (~5–7 wt%) water contents are highly evolved (~70–74 wt% SiO_2) in all samples, regardless of whole-rock composition. This suggests that high-H_2O pyroxene-hosted melt inclusions in low-silica magmas did not necessarily form from those low-silica magmas.

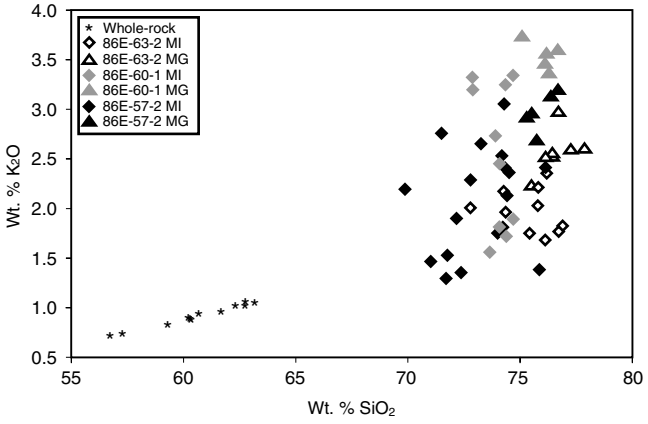

Fig. 9 K_2O vs. SiO_2 for all compositional analyses. *Asterisks* represent whole-rock analyses (Table 2), *diamonds* represent melt inclusion (MI) analyses (Tables 3 and 7, normalized anhydrous), and *triangles* represent matrix glass (MG) analyses (Table 8). *Open symbols* = 86E-63-2, *gray symbols* = 86E-60-1, *black symbols* = 86E-57-2

Augite and orthopyroxene cores with similar compositions are found in all three of our samples (Fig. 7), and reverse zoning of pyroxene phenocrysts occurs in the two mafic samples. Based on these observations, we suggest that some of the pyroxene phenocrysts (along with melt inclusions) in the mixed magmas erupted in 1986 are inherited from the dacitic endmember, which had been stored beneath Augustine since 1976. This indicates that the most mafic sample (86E-57-1) is not representative of an unmixed parental magma, as it also contains inherited pyroxene phenocrysts. Therefore, the mafic parental magma was either incorporated completely into the dacitic magma during mixing or overlooked during our sampling efforts.

Relative timing of magma mixing, ascent, and crystallization

The occurrence of post-mixing crystallization is indicated by changing core-to-rim pyroxene compositions in low-silica samples (Fig. 7), by the compositional continuum between melt inclusions and matrix glasses (Fig. 9), and by re-equilibration or re-crystallization of Fe-Ti oxides. Post-mixing phenocryst crystallization, along with melt inclusion entrapment, may have occurred as magmas ascended towards the vent, leading to the observed range in melt inclusion volatile contents. Alternatively, it is possible that some melt inclusions trapped prior to magma ascent subsequently leaked volatiles. To investigate the origin of the analyzed melt inclusions, we plot melt inclusion H_2O vs. K_2O and SiO_2 for all samples (Fig. 10), and couple those with observations of groundmass textures (Fig. 11).

Individual samples appear to have different post-mixing crystallization histories, although all preserve evidence of varying degrees of crystallization during ascent. The silicic sample, 86E-63-2, appears to have a simple crystallization history. Apart from two anomalous inclusions which may have leaked volatiles during ascent, trends in K_2O and SiO_2 with water loss are roughly linear for combined melt inclusion and matrix glass data and indicative of crystallization during volatile loss. Both trends have steep slopes, indicating only a small degree of crystallization with water loss. This is consistent with the observed low microlite crystallinity of this sample (Fig. 11c). Decompression-induced crystallization at low pressures is dominated by nucleation (microlite formation). However, Hammer and Rutherford (2002) find that growth of existing crystals may occur simultaneously, leading to continuous entrapment of melt inclusions whose compositions reflect groundmass crystallization. The intermediate composition sample, 86E-60-1, has a shallow linear trend of increasing K_2O with decreasing H_2O for melt inclusions and matrix glass, indicating a greater degree of crystallization during ascent. However, there is no corresponding change in SiO_2 with decreasing H_2O, and the matrix glasses have higher SiO_2 for similar H_2O contents than inclusions (Fig. 10). Relatively slow diffusion of SiO_2 compared to K_2O in the melt phase of the intermediate sample (86E-60-1) may account for the compositional offset between melt inclusion and matrix glasses (e.g., Michael et al. 2002), or the H_2O-SiO_2 trend may reflect the shallow precipitation of plagioclase and quartz (e.g., Martel and Schmidt 2003), for which we find some textural evidence (Fig. 11b). The crystallization history of the mafic sample, 86E-57-2, is least clear. The absence of a simple crystallization history in this sample may be at least partially due to the xenocrystic origin of some pyroxene melt inclusion host crystals and the mixed nature of this magma. Processes occurring in this magma are less clear from the plot of SiO_2 vs. H_2O, although the spread of the data is consistent with multiple processes (e.g., mixing and crystallization) occurring during ascent.

Samples from the 1986 eruption of Augustine present evidence for a relationship between crystallinity and whole-rock composition. Although samples from the explosive phase have a wide range in whole-rock compositions, there is only a small range in matrix glass compositions, indicating that mafic samples are more crystalline than silicic samples. This observation is consistent with observed groundmass textures showing high microlite crystallity in andesitic samples and low microlite crystallinity in dacitic samples (Fig. 11). A similar correlation between whole-rock composition and groundmass crystallinity has been identified in the compositionally diverse products of the 1990 eruption of Redoubt Volcano, Alaska (Wolf and Eichelberger 1997) and the 1953-1974 eruption of Southwest Trident Volcano, Alaska (Coombs et al. 2000). It seems likely that the extent of microlite crystallization in response to H_2O loss during ascent is controlled by magma composition. Alternatively, it is possible that mixing of cooler, residual dacite with mafic magmas induced crystallization in these samples during mixing and ascent, and that the low microlite crystallinity of unmixed magmas is simply a function of their undisturbed cooling history.

Conclusions

Magmas erupted in 1986 at Augustine Volcano, Alaska are compositionally heterogeneous, with whole-rock compositions ranging from basaltic andesite to dacite, and are the product of mixing between a cooler dacitic magma, probably the residual from the 1976 eruption, and a hotter, newly injected mafic magma. The mixing event preceding the 1986 eruption of Augustine differs from many other mixing events in that the entire compositional range produced in the initial phase of the eruption persists through the later (effusive) stages of the eruption with little evidence of homogenization.

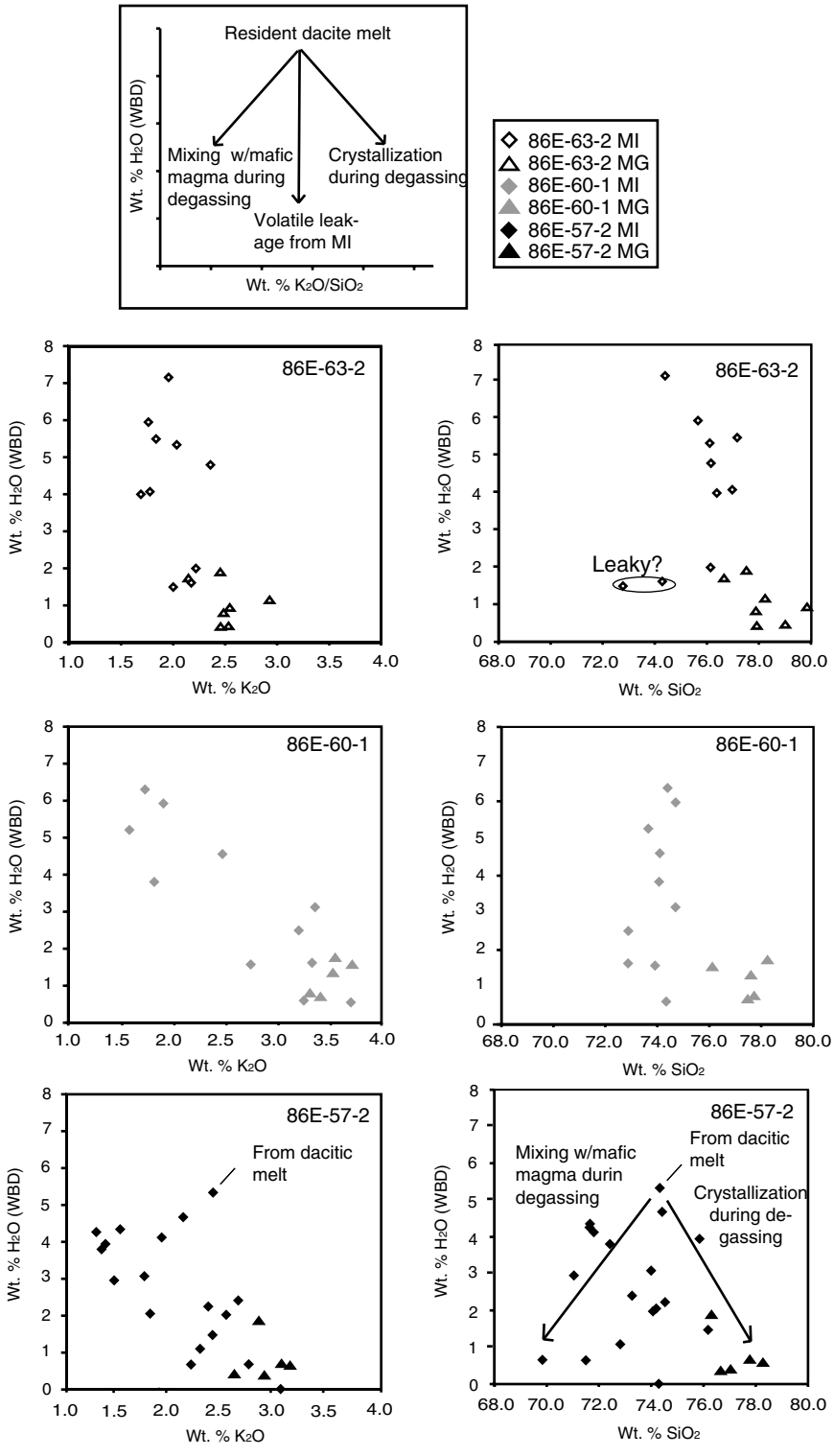

Fig. 10 H_2O content of melt inclusions and matrix glass (det. by WBD method) vs. K_2O and SiO_2 (wt%, normalized) for individual samples. *Diamonds* represent melt inclusion data and *triangles* represent matrix glass data. All data from Tables 3 and 7 are plotted. *Inset* shows expected paths for mixing during ascent, melt inclusion leakage, and continuous entrapment during ascent

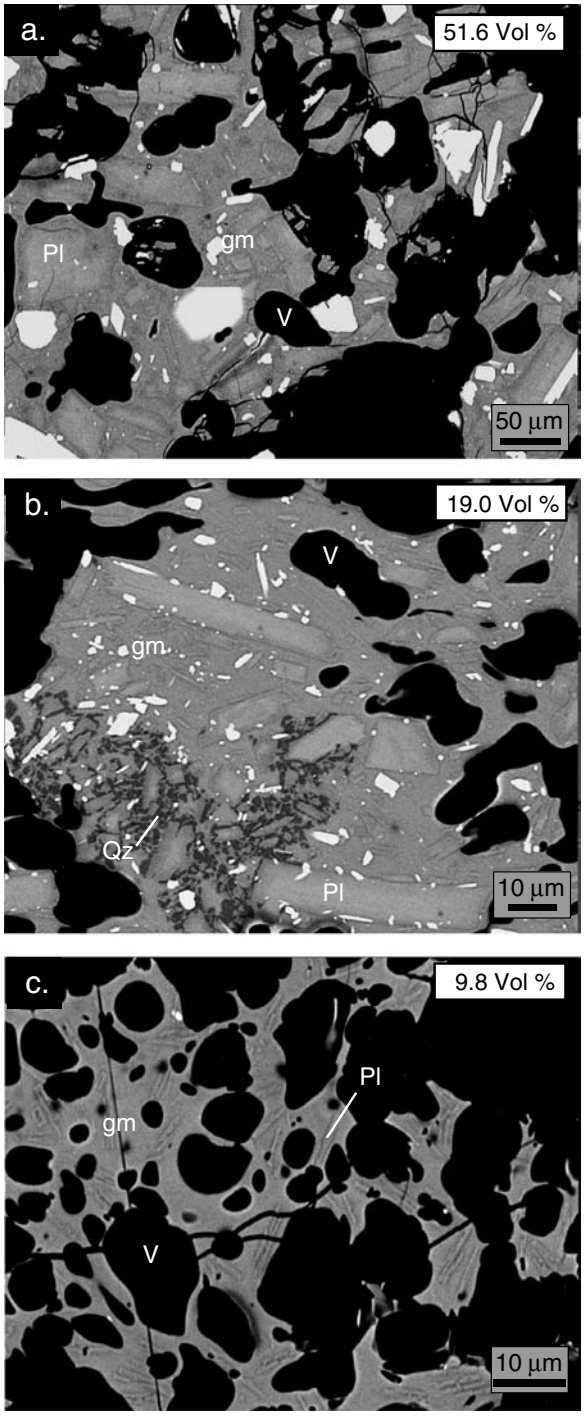

Fig. 11 BSE images showing groundmass textures of pumiceous pyroclastic flow samples. Note decreasing microlite crystallinity (vol%) with increasing SiO_2 content: **a** 86E-57-2 (57.3 wt% SiO_2, 250x), **b** 86E-60-1 (60.2 wt% SiO_2, 1000x), **c** 86E-63-2 (62.8 wt% SiO_2, 1500x). *Pl*=plagioclase; *V*=vesicle; *gm*=groundmass, *Qz*=quartz

We propose that storage and mixing took place in a network of dikes that prevented progressive chemical homogenization through the course of this eruption. The addition of new magma to the storage region may have destabilized the region and initiated the onset of the eruption. Furthermore, it is possible that systems such as Augustine that experience frequent small injections and eruptions of new magma are more likely to retain a complex storage system, since long repose intervals would allow such a system of small dikes to freeze. Similar dike-like storage systems may be common to other volcanoes in the Cook Inlet region of Alaska where short repose periods and compositionally heterogeneous magmas are also observed.

The 1986 Augustine magmas have a complex crystallization history related to mixing processes. Observed trends of decreasing melt inclusion H_2O with decreasing K_2O and SiO_2 in some indicate that mixing to form intermediate to mafic whole-rock compositions may have continued during magma ascent. Based on melt inclusion analyses and textural evidence, we also observe a correlation between the degree of groundmass crystallization and whole-rock composition, consistent with recent experimental data indicating that the extent of decompression-driven crystallization is controlled by both the composition of the melt phase and conditions of decompression (Hammer and Rutherford 2002; Martel and Schmidt 2003).

Acknowledgements We are extremely grateful for assistance and input from Carrie Brugger, Dana Johnston, and Stacey Hager, and for constructive reviews from Jake Lowenstern, Michelle Coombs, James D. Myers, and Mike Carroll. This work was funded by NSF grant EAR-9909507 to K. Cashman and D. Johnston, and by the USGS Volcano Hazards Program.

References

Anderson DJ, Lindsley DH, Davidson PM (1993) QUILF: A Pascal program to assess equilibria among Fe-Mg-Mn-Ti oxides, pyroxenes, olivine, and quartz. Comp Geosci 19:1333–1350

Anderson DJ, Lindsley DH (1988) Internally consistent solution models for Fe-Mg-Mn-Ti oxides: Fe-Ti oxides. Am Mineral 73:714–726

Bacon CR, Hirschmann MM (1998) Mg/Mn partitioning as a test for equilibrium between coexisting Fe-Ti oxides. Am Mineral 73:57–61

Blank JG, Stolper EM, Carroll MR (1993) Solubilities of carbon dioxide and water in rhyolitic melt at 850 degrees C and 750 bars. Earth Planet Sci Lett 119:27–36

Cioni R, Civetta L, Marianelli P, Metrich N, Santacroce R, Sbrana A (1995) Compositional layering and syn-eruptive mixing of a periodically refilled shallow magma chamber, the AD 79 Plinian eruption of Vesuvius. J Petrol 36:739–776

Coombs ML, Eichelberger JC, Rutherford MJ (2000) Magma storage and mixing conditions for the 1953–1974 eruptions of Southwest Trident volcano, Katmai National Park, Alaska. Contrib Mineral Petrol 140:99–118

Cribb JW, Barton M (1997) Significance of crustal and source region processes on the evolution of compositionally similar calc-alkaline lavas, Mt. Hood, Oregon. J Volcanol Geotherm Res 76:229–249

Daley EE (1986) Petrology, geochemistry, and the evolution of magmas from Augustine Volcano, Alaska. MS Thesis, University of Alaska, Fairbanks, 106 pp

Devine JD, Gardner JE, Brack HP, Layne GD, Rutherford MD (1995) Comparison of microanalytical methods for estimating H_2O contents of silicic volcanic glasses. Am Mineral 80:319–328

Donovan JJ, Tingle TN (1996) An improved mean atomic number correction for quantitative microanalysis. J Microscopy 2:1–7

Eichelberger JC, Chertkoff DG, Dreher ST, Nye CJ (2000) Magmas in collision: rethinking chemical zonation in silicic magmas. Geology 28:603–606

Gardner CA, Cashman KV, Roman DC (2000) Decreasing magma ascent rates inferred from groundmass textures during the 1986 eruption of Augustine Volcano, Alaska. Geol Soc Am Abstr 32:A-111

Gourgaud A, Fichaut M, Joron J-L (1989) Magmatology of Mt. Pelée (Martinique, F.W.I.), I: magma mixing and triggering of the 1902 and 1929 Pelean nuées ardentes. J Volcanol Geotherm Res 38:143–169

Hammer JE, Rutherford MJ (2002) An experimental study of the kinetics of decompression-induced crystallization in silicic melt. J Geophys Res 107:ECV8–1-8-24

Harris G (1994) The petrology and petrography of lava from the 1986 eruption of Augustine Volcano. Thesis, University of Alaska, Fairbanks, 131 pp

Hildreth W, Fierstein J (2000) Katmai volcanic cluster and the great eruption of 1912. Geol Soc Am Bull 112:1594–1620

Hildreth W (1983) The compositionally zoned eruption of 1912 in the Valley of Ten Thousand Smokes, Katmai National Park, Alaska. J Volcanol Geotherm Res 18:1–56

Huebner JS, Sato M (1970) The oxygen fugacity-temperature relationships of manganese oxide and nickel oxide buffers. Am Mineral 55:934–952

Johnston DA (1978) Volatiles, magma mixing, and the mechanism of eruption of Augustine Volcano, Alaska. Dissertation, University of Washington, 177 pp

Kienle J (1987) Mt. St. Augustine works, but how? Proceedings, Hawaii Symposium on How Volcanoes Work, p 139

Lowenstern JB (1994) Chlorine, fluid immiscibility, and degassing in peralkaline magmas from Pantelleria, Italy. Am Mineral 79:353–369

Martel C, Schmidt BC (2003) Decompression experiments as an insight into ascent rates of silicic magmas. Contrib Mineral Petrol 144:397–415

Metrich N, Rutherford MJ (1992) Experimental study of chlorine behavior in hydrous silicic melts. Geochim Cosmochim Acta 56:607–616

Michael PJ, McDonough WF, Nielsen RL, Cornell WC (2002) Depleted melt inclusions in MORB plagioclase: messages from the mantle or mirages from the magma chamber? Chem Geol 183:43–61

Newman S, Stolper E, Epstein S (1986) Measurement of water in rhyolitic glasses: calibration of an infrared spectroscopic technique. Am Mineral 71:1527–1541

Newman S, Epstein S, Stolper E (1988) Water, carbon dioxide, and hydrogen isotopes in glasses from the ca. 1340 A.D. eruption of the Mono Craters, California: constraints on degassing phenomena and initial volatile content. J Volcanol Geotherm Res 35:75–96

Nye CJ, Swanson SE, Avery VF, Miller TP (1994) Geochemistry of the 1989–1990 eruption of Redoubt Volcano: Part I. Whole-rock major- and trace-element chemistry. J Volcanol Geotherm Res 62:429–452

Ochs FA, Lange RA (1999) The density of hydrous magmatic liquids. Science 283:1314–1317

Power JA (1988) Seismicity associated with the 1986 eruption of Augustine Volcano, Alaska. Thesis, University of Alaska, Fairbanks, 142 pp

Reagan MK, Gill JB, Malavassi E, Garcia MO (1987) Changes in magma composition at Arenal Volcano, Costa Rica, 1968-1985: real-time monitoring of open-system differentiation. Bull Volcanol 49:415–434

Roman DC (2001) The 1986 eruption of Augustine Volcano, Alaska: Magma Storage and Ascent. MS Thesis, University of Oregon, 129 pp

Streck MJ, Dungan MA, Malavassi E, Reagan MK, Bussy F (2002) The role of basalt replenishment in the generation of basaltic andesites of the ongoing activity at Arenal volcano, Costa Rica: evidence from clinopyroxene and spinel. Bull Volcanol 64:316–327

Swanson SE, Kienle J (1988) The 1986 eruption of Mount St. Augustine: field test of a hazard evaluation. J Geophys Res 93:4500–4520

Tingle TN, Neuhoff P, Ostergren J, Jones RE (1996) The effect of "missing" (unanalyzed) oxygen on quantitative electron probe microanalysis of hydrous silicate and oxide minerals. Geol Soc Am Abst 28:212

Venezky DY Rutherford MJ (1999) Petrology and Fe-Ti oxide reequilibration of the 1991 Mount Unzen mixed magma. J Volcanol Geotherm Res 89:213–230

Waitt RB, Beget JE (1996) Provisional geologic map of Augustine Volcano, Alaska. US Geol Surv Open-File Rep 96–516

Wallace P, Anderson AT, Davis, AM(1999) Gradients in H_2O, CO_2 and exsolved gas in a large-volume silicic magma system: interpreting the record preserved in melt inclusions from the Bishop Tuff. J Geophys Res 104:20097–20122

Waythomas CF, Waitt RB (1998) Preliminary volcano hazard assessment for Augustine Volcano, Alaska. US Geol Surv Open-File Rep 98–106

Wolf KJ, Eichelberger JC (1997) Syneruptive mixing, degassing, and crystallization at Redoubt Volcano, eruption of December 1989 to May 1990. J Volcanol Geotherm Res 75:19–37

Yount ME, Miller TP (1987) The April 1986 eruptive phase of Augustine Volcano and associated hazards. Proceedings, Hawaii Symposium on How Volcanoes Work, p 276